

SPECIAL COLLECTION: OLIVINE

# Elastic plastic self-consistent (EPSC) modeling of plastic deformation in fayalite olivine†‡

PAMELA C. BURNLEY<sup>1,\*</sup>

<sup>1</sup>Department of Geosciences and High Pressure Science and Engineering Center, University of Nevada, Las Vegas, Nevada 89154-4010, U.S.A.

## ABSTRACT

Elastic plastic self-consistent (EPSC) simulations are used to model synchrotron X-ray diffraction observations from deformation experiments on fayalite olivine using the deformation DIA apparatus. Consistent with results from other in situ diffraction studies of monomineralic polycrystals, the results show substantial variations in stress levels among grain populations. Rather than averaging the lattice reflection stresses or choosing a single reflection to determine the macroscopic stress supported by the specimen, an EPSC simulation is used to forward model diffraction data and determine a macroscopic stress that is consistent with lattice strains of all measured diffraction lines. The EPSC simulation presented here includes kink band formation among the plastic deformation mechanisms in the simulation. The inclusion of kink band formation is critical to the success of the models. This study demonstrates the importance of kink band formation as an accommodation mechanism during plastic deformation of olivine as well as the utility of using EPSC models to interpret diffraction from in situ deformation experiments.

**Keywords:** High-pressure studies, olivine, deformation, XRD data, synchrotron X-ray, diffraction

## INTRODUCTION

High-temperature and pressure-deformation experiments are key to placing quantitative bounds on the rheology of mantle phases and thus are highly important for understanding the rheology of the mantle. Experimental work on olivine is particularly valuable because it is an important constituent of the upper mantle and likely exerts considerable control on its rheology. The high-temperature rheology of olivine has been the subject of extensive experimental research, but only in the last decade has instrumentation (Karato and Weidner 2008; Weidner et al. 2010) been available to conduct quantitative experiments at the pressures suitable to the upper mantle. These new high-pressure deformation experiments (Li et al. 2004; Chen et al. 2006; Burnley and Zhang 2008; Nishihara et al. 2008; Karato and Weidner 2008; Raterron et al. 2007, 2009, 2011, 2012, 2013; Karato 2009; Kawazoe et al. 2009, 2010; Durham et al. 2009; Mei et al. 2010; Long et al. 2011; Hilairet et al. 2012; Hustoft et al. 2013) rely on in situ synchrotron diffraction to monitor the elastic strain of lattice planes within the sample during deformation. Stress in the specimen is typically calculated from the differential lattice strains using a method developed by Singh et al. (1998), which assumes that the polycrystal is in a Reuss state of stress. However, investigators have also observed that within samples undergoing plastic flow stress levels calculated from multiple lattice planes disagree substantially (Li et al. 2004; Burnley and Zhang 2008; Mei et al. 2010; Hilairet et al. 2012), which creates significant uncertainty for determining the macroscopic load that is sup-

ported by the sample. For example Mei et al. (2010) find that the stress as calculated from the (130) (131) (112) lattice reflections of olivine differ from each other by between 25–41%. Some studies (e.g., Girard et al. 2010, 2013) rely on measurements made from an elastically deforming piston or stress sensor in line with the sample. However, due to frictional effects it is possible that there are variations between the stress in the sample and that in the stress sensor or piston. Therefore, it is most desirable to measure the stress state from the sample directly. The variation in stress states of different orientation subpopulations of crystals in a deforming materials is well known among metallurgists who use neutron diffraction to study the deformation of metals at room pressure (Turner and Tome 1994; Turner et al. 1995; Tome and Oliver 2002) and is believed to originate in the inhomogeneous distribution of stress and strain in the polycrystal due to single-crystal elastic and plastic anisotropy as well as interactions between neighboring grains. To address the elastic and plastic anisotropy of crystals that make up a polycrystal, metallurgists use elastic plastic self-consistent (EPSC) models (Turner and Tome 1994; Tome and Oliver 2002). EPSC models have also recently been applied to high-pressure deformation experiments in MgO (Li et al. 2004), quartz (Burnley and Zhang 2008), Co metal (Merkel et al. 2009), and olivine (Hilairet et al. 2012). In this paper, we further explore the application of EPSC models to the deformation of olivine at high pressure and temperature.

## EPSC MODELS

Self-consistent (SC) models, which are based on Eshelby's theory of inclusions (Eshelby 1957), can be used to estimate aggregate mechanical properties from single-crystal elastic and plastic properties. EPSC models consider the elastic and plastic behavior of large numbers of individual grains, each of which is characterized by its Euler angles as measured relative to the

\* E-mail: Pamela.Burnley@unlv.edu

†‡ Open access: Article available to all readers online. Special collection papers can be found on GSW at <http://ammin.geoscienceworld.org/site/misc/specialissuelist.xhtml>.

sample's coordinate frame. The models use the single-crystal elastic tensor and a description of all possible slip systems and mechanical twin laws for the material. Each deformation mechanism is described by a critical resolved shear stress (CRSS) and hardening parameters (Turner and Tome 1994; Tome and Oliver 2002). Each grain is treated as an elliptical inclusion within an infinite homogeneous matrix that has the average properties of all of the grains in the polycrystal. An increment of strain is applied to the homogeneous matrix, which then transmits stress to the grain. The grain responds elastically or plastically depending on its orientation and the present value of the CRSS for each slip system, while also fulfilling compatibility criteria. The CRSS changes as a function of the accumulated plastic strain in the grain as specified by a hardening law. The behavior of the homogeneous matrix is the sum of the behaviors of the remainder of the grains and must be recalculated after each grain is deformed. Thus the model iterates until it converges for each deformation step. Model output includes the macroscopic stress and strain for the aggregate, the average elastic strain for populations of grains that contribute to various diffraction peaks, and the evolution of slip system activity at each step in the calculation. The model results can be directly compared with diffraction results. The stress and strain tensor for each grain at the end of a simulation can also be extracted from the code (Tome and Oliver 2002).

The nature of the EPSC model suggests that it should be a valuable tool for interpreting diffraction data from high-pressure in situ deformation experiments and provide a superior estimate of the macroscopic load supported by the sample for many reasons. First, it does not make the demonstrably incorrect assumption of a Reuss state of stress. Second, it provides a framework for integrating disparate stress measurements. Third, it takes into account the fact that only a small fraction of the grains in the sample are measured in an in situ diffraction pattern and it integrates the contribution of the "silent" grain populations into the model result. Last but not least, the models give information about the plastic deformation mechanisms operating in the sample.

## METHOD

### Experimental technique

**D-DIA apparatus.** Deformation experiments were conducted using the D-DIA apparatus (Durham et al. 2002; Wang et al. 2003; Weidner and Li 2006; Weidner et al. 2010) located at National Synchrotron Light Source X17B2 beamline. The D-DIA apparatus compresses a cubic sample assembly using 6 hard anvils driven inward by two wedged guide blocks. Hydraulic rams incorporated in the guide blocks are used to produce controlled deformation by advancing the top and bottom anvils independent of the side anvils (Durham et al. 2002; Wang et al. 2003). The sample assemblies used for the experiments described here consisted of a boron epoxy cube surrounding a thin cylindrical graphite furnace in an alumina support sleeve. For Fay\_33, two W3%Re-W25%Re thermocouples introduced at the midpoint of the furnace were used to measure the sample temperature (Supplemental Figure 1<sup>1</sup>). For Fay\_37 the thermocouple was incorporated in the upper piston (Fig. 1). The sample, which consisted of synthetic fayalite powder, was enclosed in a 25  $\mu\text{m}$  thick Ni metal jacket and surrounded by a confining medium sleeve; for Fay\_33 the sleeve consisted of NaCl mixed with 10% BN, for Fay\_37 it consisted of 100% BN. Crushable alumina pistons were used to transmit the load from the

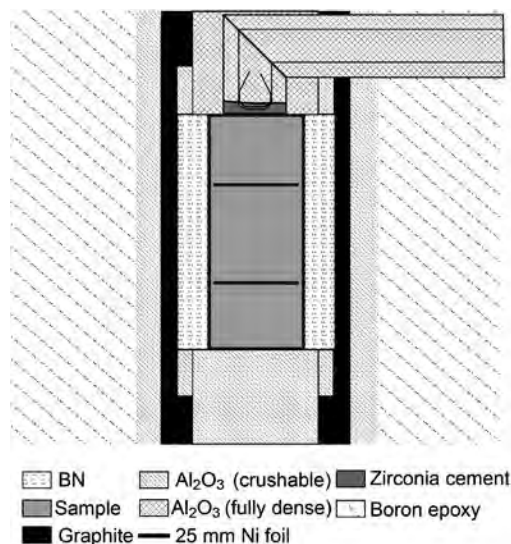


**FIGURE 1.** Sample assembly for Fay\_37. The pressure medium consists of a 6 mm cube of boron epoxy. The interior consists of nested sleeves surrounding a cylindrical sample. The thermocouple is introduced axially via a trough across the top of assembly. The function of each material included in the assembly is discussed in the text.

top and bottom anvils to the sample. Several 25  $\mu\text{m}$  thick Ni foils packed within the powdered specimen, were used as strain markers. Experiments were compressed cold to  $\sim 4.0$  GPa and annealed at high temperature for one hour, which produced an aggregate with  $\sim 10$   $\mu\text{m}$  grain size. The temperature was then lowered to the experimental temperature and final adjustments to the pressure were made if needed. Conditions for the experiments are given in Table 1.

**In situ X-ray measurements.** The D-DIA is positioned such that the synchrotron X-ray beam can enter the sample assembly via the gap between two of the side anvils. A transparent anvil is used on the downstream side to allow the diffracted X-rays to be observed at various angles. An array of energy-dispersive detectors is used to collect the diffracted X-rays. A conical slit, which sits up-stream of the detectors, determines the two  $\theta$  angle of the diffracted X-rays and eliminates diffraction from the sample assembly. Because the X-ray source is white, there will be a wavelength that fulfills the Bragg condition for each set of lattice planes in the sample. Thus each detector measures a full powder pattern from the sample. Experiment Fay\_33 was conducted with the slit system described in Durham et al. (2002) and Burnley and Zhang (2008), Fay\_37 was conducted with a conical slit system (Weidner et al. 2010) (Fig. 2). Diffraction collected from the detectors for which  $\psi = 0^\circ$  and  $180^\circ$  is referred to as being measured in the compression direction. Diffraction measured with  $\psi = 90^\circ$  and  $270^\circ$  is referred to as having been measured in the transverse direction. Lattice spacings were determined from the diffraction pattern via calibration spectra that were collected at the start of each experiment. Additional details about the X-ray measurements can be found in Burnley and Zhang (2008), Mei et al. (2010), and Weidner et al. (2010). Strain in the sample was measured by comparing the length of the sample in radiographic images made from the transmitted X-ray beam (Vaughan et al. 2000) as recorded by a fluorescent YAG screen located at the center of the conical slit. The starting length of the samples was recorded at the pressure and temperature conditions of the experiment immediately before the rams began advancing for the deformation.

**TABLE 1.** Experimental conditions

	Temperature anneal ( $^\circ\text{C}$ )	Temperature deformation ( $^\circ\text{C}$ )	Pressure (GPa)	Strain rate	Total strain
Fay_33	$800 \pm 20$	$682 \pm 15$	$3.5 \pm 0.4$	$1 \times 10^{-5}$	8.8%
Fay_37	$770 \pm 50$	$26 \pm 1$	$2.70 \pm 0.05$	$2 \times 10^{-5}$	15.4%

*Notes:* Uncertainty in temperature is based on observed temperature variation during experiment. The hot spot and thermocouple temperature may differ by  $\sim 50$   $^\circ\text{C}$ . The annealing temperature for Fay\_37 is estimated based on furnace power. Uncertainty in pressure includes both uncertainty in measured  $d$ -spacings and propagated temperature uncertainty.

<sup>1</sup> Deposit item AM-15-75234, Figures and tables. Deposit items are free to all readers and found on the MA web site, via the specific issue's Table of Contents (go to <http://www.minsocam.org/MSA/AmMin/TOC/>).

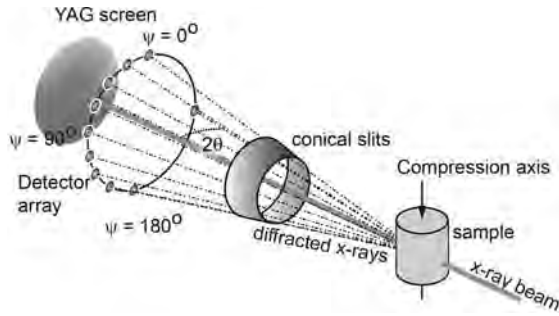


**FIGURE 2.** Diffraction geometry for D-DIA experiments. For clarity, the apparatus is not shown but the direction of the compression axis and the sample are shown along with the orientation of the incoming X-ray beam and the position of the 10 detectors and the YAG screen. The conical slit that excludes X-rays diffracting at angles other than  $2\theta$  is shown schematically.

Spectra collected while the D-DIA motors were not running were collected for 300 s each. Alternating sets of five 60 s spectra from the sample and radiographs were taken throughout the deformation portion of the experiment. For initial analysis, the intensity vs. channel data from each of the spectra were summed to make the equivalent of a 300 s spectra. For portions of the experiment where lattice strains were changing rapidly, the individual spectra were analyzed. Otherwise, the summed spectra were used for peak fitting. Typically D-DIA results are analyzed by calculating a differential lattice strain ( $\epsilon^{hkl}$ ) (Singh et al. 1998) from the difference between the  $d$ -spacing as measured in the compressional ( $c$ ) and transverse ( $t$ ) detectors:

$$\epsilon^{hkl} = (d_t^{hkl} - d_c^{hkl}) / d_p^{hkl}$$

where  $d^{hkl} = (d^{hkl} + 2d^{hkl})/3$  and  $d_t^{hkl}$  and  $d_c^{hkl}$  are the measured  $d$ -spacings for a given set of lattice planes. This technique allows  $d_t^{hkl}$  and  $d_c^{hkl}$  to be modeled using diffraction data taken from all values of  $\psi$  (Hilair et al. 2012). However, implicit in the calculation of differential lattice strain is the assumptions that the material is in a Reuss state of stress. To avoid this assumption we calculate the lattice strain  $\epsilon^{hkl} = (d^{hkl} - d_0^{hkl})/d_0^{hkl}$  where  $d_0^{hkl}$  is the lattice constant measured immediately before the beginning of deformation for each detector. The pressure is kept constant during the experiment by a computer monitored feedback system that allows the side anvils to retract during deformation. Thus normalizing by the hydrostatic pressure is not required. This strategy also eliminates systematic offsets due to small differences in the calibration of each energy-dispersive detector.

## EPSC models

To interpret diffraction data collected with the D-DIA, it was compared with simulated diffraction data generated with an EPSC model. An EPSC code (EPSC3) provided by C.N. Tome (Tome and Oliver 2002) was used; with some modifications as discussed below. Cell dimensions and single-crystal elastic constants for the models were calculated for the pressure temperature conditions appropriate to each experiment using values from Smyth and Hazen (1973), Speziale et al. (2004), and Isaak et al. (1993). To simulate experiments in the D-DIA, which was operated at a constant strain rate, numerical experiments were run with a uniaxial strain boundary condition. Compressive strain was used as the control variable. Strain in the transverse directions as well as all stresses were allowed to vary freely. Changes in confining pressure during compression were not included in the models, which is appropriate because the pressure was not allowed to increase during DDIA experiments. Models were run to a maximum of 14% compressive strain calculated over 900 displacement increments. To obtain the degree of plastic strain remaining in each grain as well as the overall plastic strain in the polycrystal at the end of compression, an unloading stage was simulated. Unloading was simulated by ramping the stress boundary condition in the compression direction to zero in 100 increments. All strains and the transverse stresses were allowed to vary freely during unloading. The eight slip systems commonly observed in olivine as well as three unidirectional slip systems to simulate the formation of kink bands were used to describe plastic deformation of olivine (Table 2).

Olivine does not have a sufficient number of linearly independent slip sys-

tems to satisfy the von Mises criteria for arbitrary shape change. Therefore, at temperatures where the only deformation mechanism available is slip, kink bands form as an accommodation mechanism (Burnley et al. 2013, Raleigh 1968, and references therein). Kink bands form in olivine grains for which either the [100] or the [001] direction is parallel to compression (Ave Lallemand 1985; Carter et al. 1968; Raleigh 1968); however there is a spread in the orientations of grains affected by kinking (Burnley et al. 2013). Therefore unidirectional slip systems, which will affect grains in nearby orientations as well as those most ideally oriented for slip, can serve to model the modification of the single crystal yield surface produced by kink band formation. Slip on the (405) and (120) planes, which are very close to  $45^\circ$  from [100] and [001], weaken the same grains that are most likely to develop kink bands. (405)[504] and (405)[504] were used to weaken grains with [001] near the compression direction and (120)[210], (120)[210], (405)[504], and (405)[504] were used to weaken grains with [100] near the compression direction. Burnley et al. (2013) observed that in a germanate olivine polycrystal, kink bands can form in grains whose orientations deviate as much as  $35^\circ$  away from the optimal orientation. Thus the use of unidirectional slip systems will actually weaken a somewhat smaller population than will be affected by kinking. The unidirectional slip systems are also listed in Table 2.

The EPSC model uses a Voce hardening law to describe the evolution of the critical resolved shear stress ( $\tau$ ) with shear strain ( $\Gamma$ ) as follows:

$$\tau = \tau_0 + (\tau_1 + \phi_1 \Gamma) [1 - \exp(-\phi_0 \Gamma / \tau_1)]$$

where  $\tau_0$  is the initial critical resolved shear stress and  $\tau_1$ ,  $\phi_0$ , and  $\phi_1$  are hardening parameters (Turner and Tome 1994). The value of  $\tau_0$ ,  $\tau_1$ ,  $\phi_0$ , and  $\phi_1$  used in each model are listed in Table 2. For the purpose of comparing the effect of each slip system, simulations were run with values of the critical resolved shear stress and hardening parameters as follows:  $\tau_0 = 1.5$ ,  $\tau_1 = 0.5$ ,  $\phi_0 = 0.01$ , and  $\phi_1 = 0.01$ . For each model, lattice strains for several diffraction peaks that were observed in the D-DIA deformation experiments on olivine were modeled; including the (021), (101), (120), (002), (131), (112), (134), and (192) reflections observed in fayalite experiments as well as the (130) and (122) reflections, which are commonly observed in forsterite experiments.

During our initial olivine trials with the EPSC3 code we noticed that the results were dependent upon the order in which the slip systems were listed in the input file. Lattice strains from nominally identical experiments were found to differ by as much as 5%. These discrepancies were caused by the way in which versions of the code from 2002 and before dealt with combinations of slip systems that are singular (C. Tome, personal communication). In consultation with C. Tome,

**TABLE 2.** Parameters for EPSC simulations

	$\tau_0$	$\tau_1$	$\phi_0$	$\phi_1$	Macro stress (GPa) <sup>a</sup>
Comparison simulations					
(010)[100], (001)[100], {011}[100], {021}[100], {031}[100], {110}[001], (010)[001], (100)[001], and Kink systems <sup>b</sup>	1.5	0.5	0.01	0.01	
Fay_37–22					–2.77
(010)[100]	1.0	0.01	0.2	0.01	
(001)[100]	1.7	0.01	0.2	0.01	
{011}[100], {021}[100]	1.7	0.01	0.2	0.01	
{031}[100]	1.7	0.01	0.2	0.01	
{110}[001], (010)[001]	1.0	0.01	0.2	0.01	
(100)[001]	$\infty$				
Kink systems <sup>b</sup>	0.62	0.01	0.5	0.01	
Fay_37–16					–2.70
(010)[100]	1.2	0.01	0.2	0.01	
(001)[100]	1.2	0.01	0.2	0.01	
{011}[100], {021}[100]	1.2	0.01	0.2	0.01	
{031}[100]	1.2	0.01	0.2	0.01	
{110}[001], (010)[001]	1.1	0.01	0.2	0.01	
(100)[001]	1.1	0.01	0.2	0.01	
Kink systems <sup>b</sup>	0.58	0.01	0.5	0.01	
Fay_33–11					–0.71
(010)[100]	0.18	0.001	0.01	0.01	
(001)[100]	0.18	0.001	0.01	0.01	
{011}[100], {021}[100]	0.18	0.001	0.01	0.01	
{031}[100]	$\infty$				
{110}[001], (100)[001], (010)[001]	0.001	0.001	0.01	0.01	
Kink systems <sup>b</sup>	0.39	0.001	0.01	0.01	

<sup>a</sup> See Supplementary Table 1<sup>1</sup>.

<sup>b</sup> [210] on (120), [210] on (120), [504] on (405) and [504] on (405).

modifications were made to the subroutine G\_MODULUS to remedy this problem.

Another factor that influences the reliability of the output from the code is the orientation distribution of grains used in the input. The EPSC code derives the macroscopic stress by averaging the stresses in all grains in the model. To simulate a randomly oriented polycrystal, Burnley and Zhang (2008) created a grain input file with 5000 sets of Euler angles generated by a random number generator. Although the Euler angles were random, the grain orientations were not homogeneously distributed throughout orientation space. The resulting simulations lacked cylindrical symmetry. We therefore adopted an input file with 49 108 grains that were evenly distributed through Euler space with a  $5^\circ$  spacing. This input model produced the desired cylindrical symmetry in the model results.

## RESULTS

### Experimental results

Lattice strain data from experiments Fay\_33 and Fay\_37 are shown in Figure 3. Both experiments have yielded fully at  $\sim 2\%$  strain and do not work harden. There are several significant differences between the two experiments. First, as expected the lattice strains [with the exception of the (002) reflection] are roughly five times greater for Fay\_37 ( $26^\circ\text{C}$ ) than for Fay\_33 ( $682^\circ\text{C}$ ), reflecting the higher stresses supported at room temperature. Second, the relative deflection of the (002) relative to the other diffraction peaks is completely reversed between the two experiments. Finally, even during the initial increments of strain, the high-temperature experiment does not exhibit fully elastic behavior. For reference, the self-consistent elastic behavior (calculated with EPSC3 code) is plotted in Figure 3 as a gray band. The effect of temperature as well as the difference between individual lattice strains fall within the width of the band. Diffraction measured in the transverse direction exhibits lower lattice strains and is somewhat noisier than diffraction measured in the compression direction. For the compressional

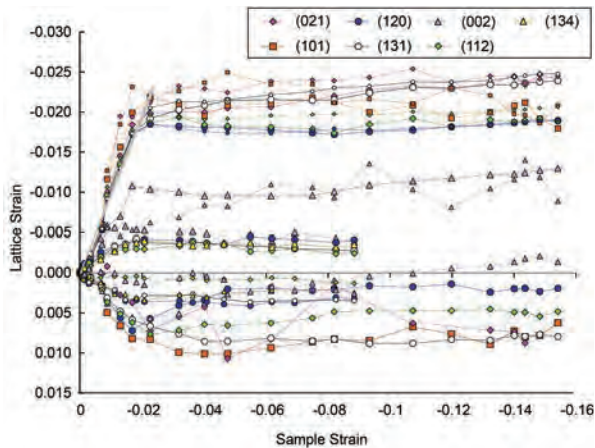


**FIGURE 3.** Lattice strain vs. sample strain for experiments Fay\_33 ( $682^\circ\text{C}$ ) and Fay\_37 ( $26^\circ\text{C}$ ). Compression produces a decrease in the lattice spacing and negative lattice strain. Lattice strains in the transverse direction (measured at  $\psi = 90^\circ$ ) are positive. For Fay\_37 negative values plotted with larger symbols are for diffraction measured at  $\psi = 180^\circ$ , smaller symbols indicate diffraction measured at  $\psi = 0^\circ$ . For Fay\_33 the average of the values measured at  $\psi = 180^\circ$  and  $\psi = 0^\circ$  are plotted. For reference, the gray band indicates the self-consistent elastic slope for all reflections plotted. Variations between individual reflections as well as the difference between the high-temperature and room-temperature slope, fit within the thickness of the band.

direction the degree of dispersion in lattice strain between reflections reaches its maximum early, and then remains relatively constant although there continues to be some variation between individual  $d$ -spacings.

### EPSC models

To facilitate the application of the EPSC models to the experimental result reported here as well as in other studies, a systematic study of the effect of each slip system on lattice strain and the interaction of slip systems was conducted.

**Single slip systems.** First the effect of each slip system operating in isolation on the lattice strain exhibited by each X-ray reflection as well as the overall strength and permanent strain in the aggregate was examined. To facilitate comparison between slip systems, the same critical resolved shear stress and hardening parameters for each slip system was used. A plot of lattice strain vs. sample strain for a typical simulation of the operation of a single slip system is shown in Figure 4; in the figure only the loading phase is plotted. Initially the aggregate deforms elastically. At a strain of 0.0227, the slip system becomes active in 288 grains. The number of grains experiencing active slip increases throughout the simulation, reaching 29 077 at the final strain of 0.14. Notice that many of the lattice strain curves do not deflect very much from their original elastic slope. This is because most of the grains in the aggregate are not well oriented for slip and either slip very little or essentially remain elastic throughout the simulation. The results for all eight slip systems, the simulated kink band system and a simulation in which no slip systems operate (labeled “elastic”) are shown in Figure 5. To facilitate comparisons between the simulations, the results are summarized by plotting the value of the lattice strain at a fixed macroscopic strain (0.14) for each simulation. The final macroscopic strength and plastic strain after unloading are presented in Supplementary Table 1<sup>1</sup>.

Each slip system produces a specific pattern of relative deflection away from the purely elastic case. With only a few subtle exceptions, varying the CRSS ( $\tau_0$ ) between 0.1 and 3 GPa and the hardening parameters ( $\tau_1$ ,  $\phi_0$ , and  $\phi_1$ ) over three orders of

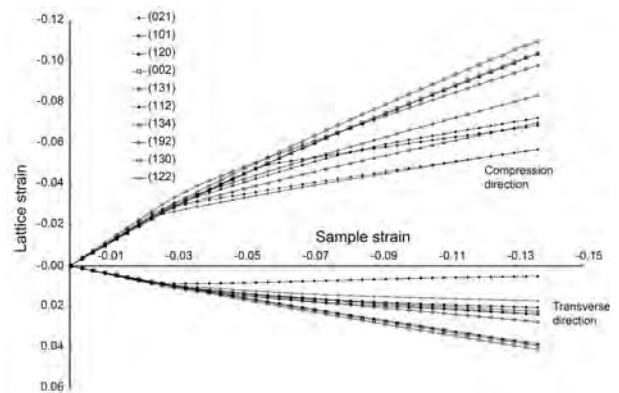


**FIGURE 4.** EPSC simulation of lattice strain vs. sample strain for the operation of the  $\{110\}[001]$  slip system. Compression produces a decrease in the lattice spacing and negative lattice strain. Lattice strains in the transverse direction are positive. The onset of plastic deformation begins at  $-0.023$  strain. The model was calculated with 900 steps; for clarity, only selected points are plotted.

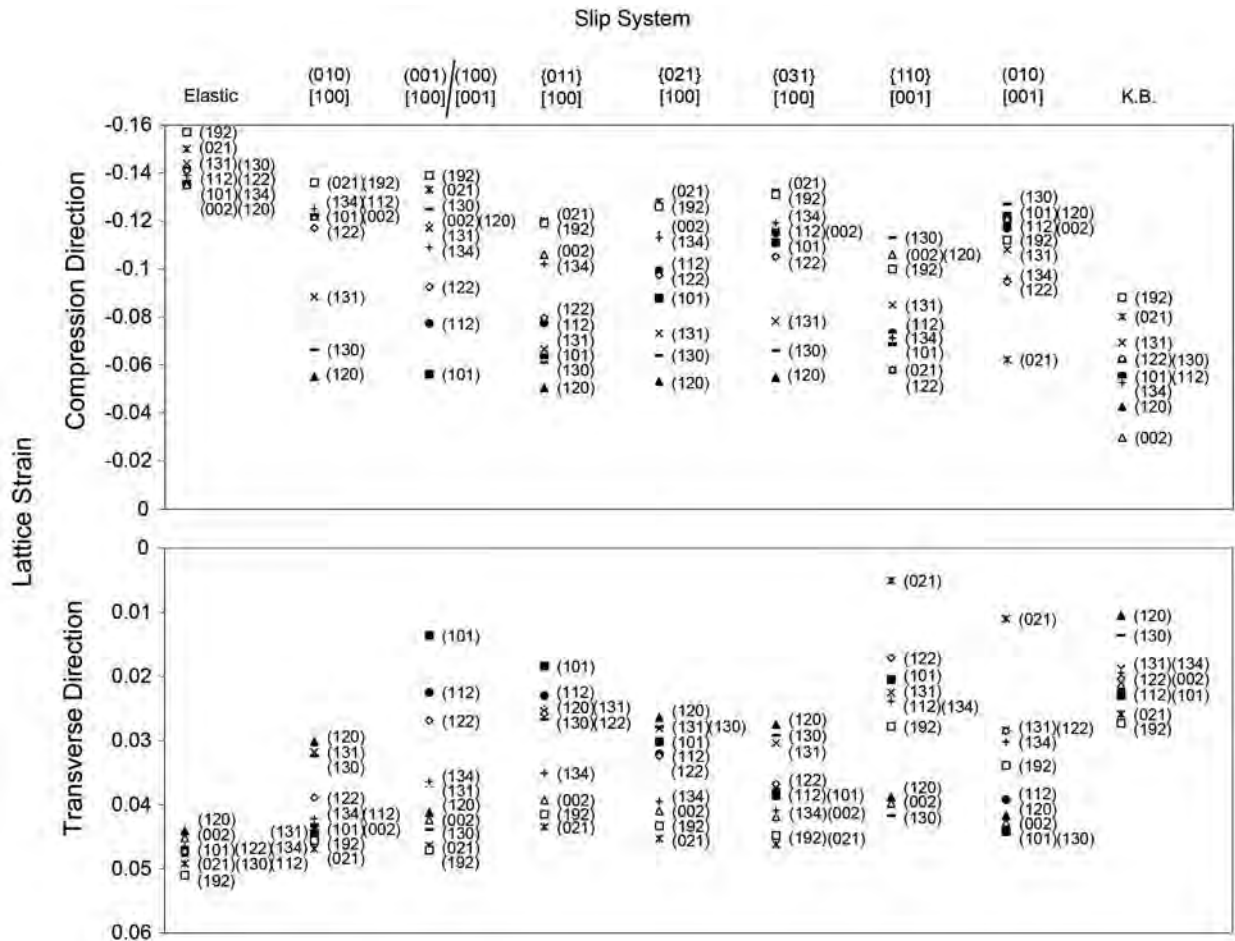


FIGURE 5. Lattice strain at 14% sample strain for EPSC simulations of the operation of individual olivine slip systems as well as a purely elastic simulation and the simulation of the kink band formation. Since the (001)[100] and (100)[001] slip systems have identical Schmidt factors, they are plotted together.

magnitude produced no change in the pattern of relative deflection produced by each slip system.

The patterns of deflection produced by the operation of each slip system show both similarities and differences. For example, [100] slip on (010), {011}, {021}, and {031} all share similar features; the (192) and (021) reflections deviate little from purely elastic deformation and the (120), (130), and (131) reflections are strongly deflected away from elastic behavior. For [100] slip on (001) the (192) and (021) reflections also deviate little from purely elastic behavior but instead the (101), (112), and (122) are most strongly deflected. For the [100] slip on {011} the behavior produced by [100] slip on (010) and (001) are in a sense combined; the (101), (112), and (122) as well as the (120), (130), and (131) are deflected from purely elastic behavior. It would therefore be relatively easy to spot the operation of [100] slip but more difficult to distinguish between the operation of [100] slip on {011}, {031}, or {021} based on diffraction data. The operation of [001] slip on {110} and (010) are the only slip systems that cause the (021) reflection to be deflected, while the (120) and (130) reflections remain elastic. As with [100] slip on {011}, [001] slip on {110} combines elements that are observed

in slip on the (100) and (010) planes. Note that the Schmid factors for [100] slip on (001) and [001] slip on (100) are the same thus the model results are identical.

Although each slip system was given the same CRSS and hardening parameters, they do not have the same effect on the macroscopic strength and permanent strain of the aggregate. In particular, slip systems with more than one slip plane (e.g., {110}) weaken the aggregate more and leave more permanent strain once the load has been released (Supplementary Table 1<sup>1</sup>).

The behavior of the reflections measured in the transverse direction is broadly symmetrical with those measured in the compression direction; reflections that are strongly deflected away from the elastic slope in the compression direction by the operation of a given slip system are strongly deflected in the transverse direction as well. The exception is for [100] slip on {011}; for which the degree of deflection for (101), (112), (120), (131), (130), and (122) in the transverse direction are different relative to each other than from what is observed in the compression direction.

The distribution of strain across grain populations also varies significantly with slip system. Figure 6 shows the distribution of

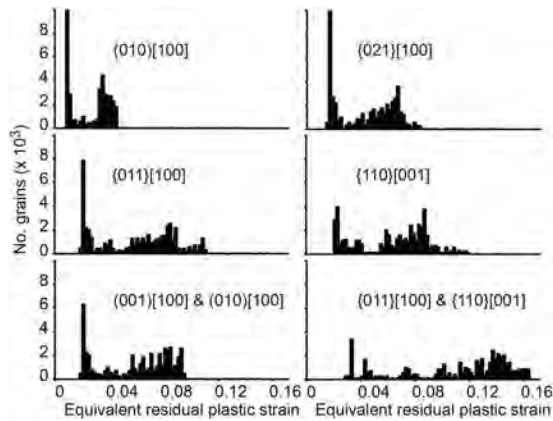


**FIGURE 6.** Histograms of residual equivalent plastic strain remaining in the sample after unloading (e.g., when the macroscopic stress has returned to zero). The slip system used for each EPSC simulation is indicated within each histogram.

equivalent plastic strain in grains after unloading. The amount of permanent strain in the grains is inversely proportional to the macroscopic stress supported by the aggregate. For even the most effective slip system, less than half of the sample strain is retained as plastic strain once the unloading phase of the simulation has brought the macroscopic stress to zero. For slip systems operating on only one plane, ~50% of the grains sustain less than 2% plastic strain. The strain distribution histograms for (010)[100] and (010)[100] and for [001] slip on (010) are very similar; the plot for (010)[100] is given in Figure 6 as an example. [100] slip on {021}, {031}, {011}, and [001] slip on {110} produce plastic strain in a larger population of grains because of the symmetrically disposed slip planes (Fig. 6).

As discussed above, to simulate kink band formation three unidirectional slip systems were used to allow plastic deformation in the population of grains that are expected to kink. Because the kink band system has several different planes and slip directions it produces much lower sample strength with more permanent strain after unloading. The pattern of deflection of X-ray reflections is distinctive from the olivine slip systems in that the (002) reflection is strongly affected by kink band formation.

**Combinations of slip systems.** Simulations for combinations of two slip systems are presented in the supplementary material (Supplemental Figure 2<sup>1</sup>). As with Figure 5, the value of the lattice strain for each reflection at sample strain of 0.14 is plotted. Combining slip systems affects the order of reflections and sample strength in variety of ways; generally the effect of the slip systems is additive. For example (010)[100] slip causes deflection of the (130), (120), and (131) reflections where (001)[100] slip most significantly affects the (101), (112), and (122) reflections. When operating together these slip systems cause all 6 of the reflections to be deflected (Fig. 7) and the macroscopic stress supported by the sample is about 25% lower. The distribution of permanent strain in the grains also shifts to higher values (Fig. 6). In contrast, the addition of (010)[100] to {031}[100] cannot be distinguished from the operation of {031}[100] alone and the addition of (010)[001] to {110}[001] cannot be distinguished from {110}[001] operating alone. This is also true of any of the

other [100] slip systems operating in combination with {011}[100], which completely dominates the pattern of lattice strains. An interesting feature of the simulations with combinations of slip systems with [100] and [001] Burgers vectors is that the pattern of broad symmetry between the transverse and normal directions deteriorates (Fig. 7).

Similarly, for combinations of three slip systems where each of the slip systems in pairs produces a lower macroscopic stress, a combination of the three produces an even lower macroscopic stress; with all three slip systems affecting the relative ordering of the lattice strain. Combinations of three that included a pair where one slip system had relatively little effect on the outcome also resulted in little change from that of the weakest set of pairs among the three. Due to this effect, combining all eight slip systems produces a result that is broadly similar to combining (010)[100], (010)[100], and (010)[001] or combining {011}[100], {021}[100], and {110}[001]. Even with all the slip systems operating the residual plastic strain after unloading is less than 50% of the maximum strain during the experiment. With the addition of the kink band formation the lowest macroscopic stresses are achieved and residual plastic strain is increased to 77% of the maximum strain.

## DISCUSSION

### Diffraction in the compression direction

Hilairret et al. (2012) compared EPSC model results with diffraction measured from San Carlos olivine in the D-DIA. These authors found that they could not match their experimental results with EPSC models; they could not reproduce the overall magnitude of the elastic strains exhibited by reflections or the lack of work-hardening behavior. They were also not able to reproduce the relative order of the reflections. As pointed out by Hilairret et al. (2012) this failure of the model is in part due to the fact that the EPSC model only examines the effect of glide and does not model climb, cross slip, or recrystallization. To examine how well the EPSC model works in the circumstance where only glide is operating, diffraction data from Fay\_37 deformed at 26 °C was simulated. The fact that the (002), (112), and (120) reflections have lower lattice strains indicates that kink band formation is playing an important role. An effort to model the data using only the slip systems produced discrepancies similar to those observed by Hilairret et al. (2012); the models work harden much more strongly than the experimental results and the relative deflection of the reflections could not be matched. The most prominent discrepancy between the diffraction data and model simulations that used only the slip systems is the behavior of the (002) reflection. As discussed above, none of the slip systems allow compression parallel the crystallographic axes of olivine to be dissipated; thus the (002) reflection should be the least deflected from its purely elastic slope. In olivine deformed both naturally and experimentally at low to moderate temperatures, the formation of kink bands allows olivine grains with their [100] and [001] axes parallel to compression to shorten (Burnley et al. 2013). As discussed above, unidirectional slip systems were implemented to allow these grain populations to deform. Utilizing the kink band simulation a significantly better match to the data in the compression direction can be obtained.

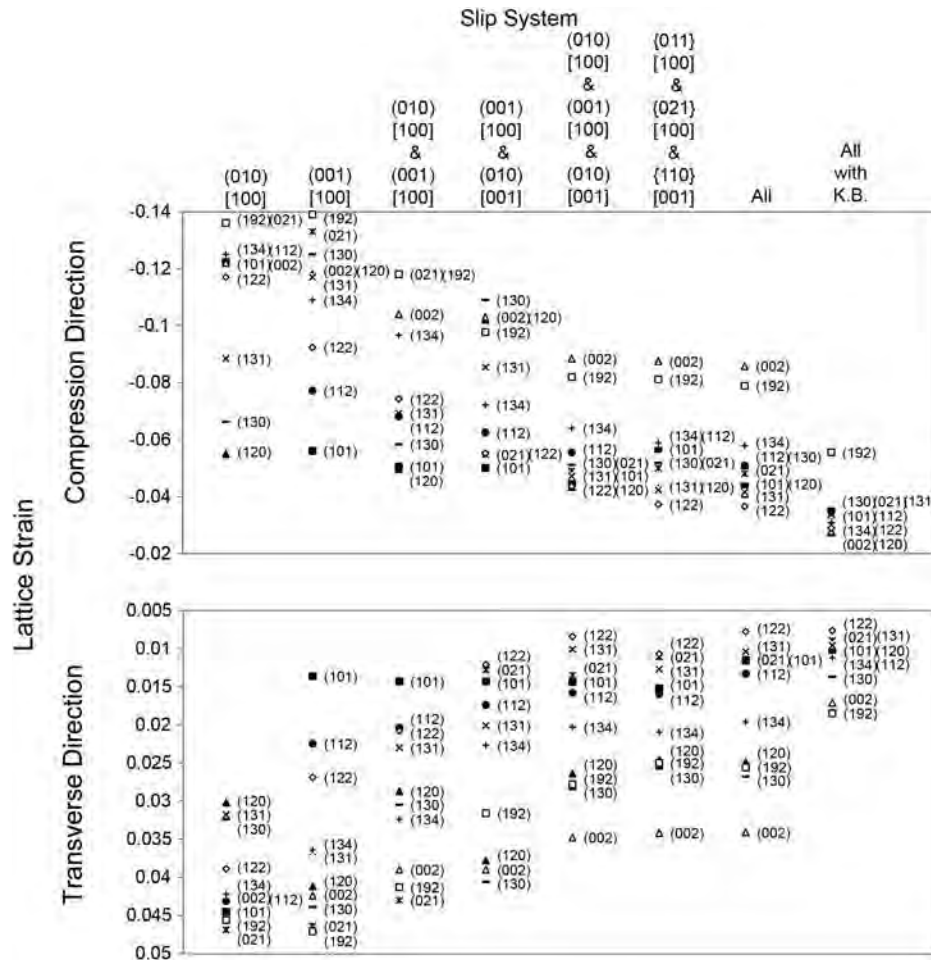


FIGURE 7. Lattice strain at 14% sample strain for EPSC simulations of the operation of various slip systems. Note that as more slip systems are added to the simulation, the level of lattice strain for all reflections declines.

Not only can the behavior of the (002) be predicted, but the combination of both the (120) and (112) reflections having lower lattice strains can also be predicted. With the addition of the other slip systems the relative order of the other reflections in the compression direction (Fig. 8) can be matched. Unlike most of the other reflections, the lattice strain of the (101) reflection in the compression direction, relative to the other reflections, changes with strain. Minor changes to the CRSS values in the EPSC simulation produces models that have the (101) follow the (131) (model Fay\_37-22 shown in Fig. 8) or the (112) (model Fay\_37-16). Thus the EPSC model can be adjusted to match the position of the (101) either at low strain (~4%) or at higher strain (~12%). The model is not capable of producing work-softening behavior, thus the behavior of the (101) reflection as a function of strain past the yield point cannot be duplicated. However, the difference between the macroscopic stress predicted by the two models is <0.1 GPa; which is ~3% of the calculated value (Table 2). The diffraction measured in the transverse direction cannot be fit by the models as closely as that measured in the compression direction, this phenomena has been noted by other workers as well (Daymond 2006; Oliver et al. 2004) and will be

discussed in more depth in the next section.

A good match between an EPSC model and the higher temperature (682 °C) diffraction data set is also obtained by using a combination of slip systems and the formation of kink bands (Fig. 9). However instead of being the weakest system, kink band formation is modeled as the strongest (Table 2). Without using the kink band simulation, the EPSC models work harden strongly and cannot match the overall behavior of the diffraction data. It is interesting to note that the CRSS for the slip systems varies by 2–3 orders of magnitude between the EPSC models for the high-temperature and the low-temperature experiments, in contrast to the CRSS for kink band formation varies by less than a factor of two. This is consistent with the hypothesis that kink band formation is a bucking instability dependent upon the elastic moduli (Budynas 1999; Burnley et al. 2013) rather than a thermally activated processes.

In addition to revealing information about the relative CRSS of various slip systems operating in the material, the use of EPSC models permits one to calculate a macroscopic stress supported by the sample that is consistent with all diffraction data rather than depending on data from a single reflection or the average of

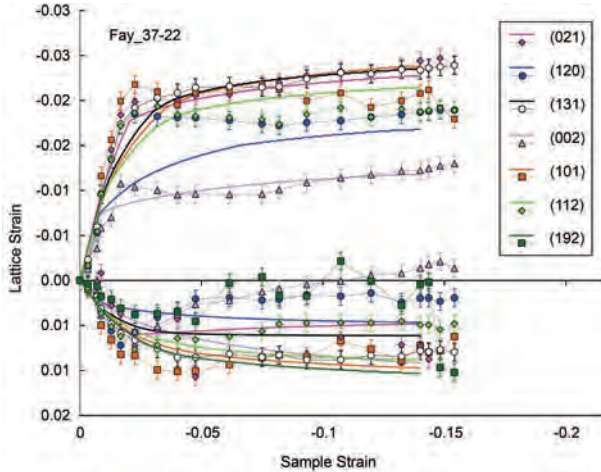


**FIGURE 8.** EPSC simulation Fay37-22 compared to lattice strains from experiment Fay\_37 (26 °C). The simulated lattice strains match the measured lattice strains to within measurement error for the (002), (131), and (021) reflections in the compression direction. The behavior of the (101) reflections deviates after 10% strain. The behavior of the (112) and (120) reflections are not matched as well but their relative position between the (002) and (131) reflections is maintained. The match of the simulation to the lattice strains in the transverse direction is not as good, as discussed in the text.

the reflections that happen to be measured. As discussed above, currently the method of determining the stress for each reflection (Singh et al. 1998) is used by most practitioners (e.g., Hilaret et al. 2012; Kawazoe et al. 2010, 2009; Mei et al. 2010; Nishihara et al. 2008). Table 3 compares the stresses obtained from the EPSC models with those obtained by using the method described by Singh et al. (1998). As can be seen in Table 3, the estimates of the macroscopic stress calculated from each reflection vary by more than a factor of two. Furthermore, the measured reflections represent only a small fraction of the grains in the sample so it would be difficult to say with confidence that the population of grains sampled by diffraction is truly representative of the entire population. There is no reason to assume that the average of the stress calculated from the measured reflections represents the average of the stress on the entire grain population. In contrast, the EPSC model simulates all of the grains in the sample so even the contribution to the strength of the silent population of grains is taken into account. Although it is clearly desirable to try to approximate the lattice strain of each reflection with the EPSC model, the macroscopic stress is not highly sensitive to the exact details of the model fit. For example, of the 25 models built to simulate the room-temperature experiment, 14 had at least one point in the model where each simulated reflection was within 0.002 in lattice strain of some portion of the post yield reflection that it was simulating. The difference between the highest and lowest macroscopic stress among these models was 0.22 GPa, a little under 10% of the calculated macroscopic stress.

### Diffraction in the transverse direction

As pointed out by Burnley and Zhang (2008), the nature of the grain populations measured in the transverse and compres-

sion diffraction directions are fundamentally different. Grains contributing to diffraction in the compression direction are oriented such that they all experience the same resolved shear stress on their slip planes. In contrast, grains contributing to diffraction in the transverse direction are experiencing a variety of resolved shear stresses on their slip systems depending on how each grain is oriented (Fig. 10). To investigate this further we calculated the equivalent stress for grains in the EPSC models that compose each of the diffracting populations that we studied. The equivalent stress ( $\sigma_e$ ) is defined as:

$$\sigma_e = \sqrt{\frac{1}{2}[(\sigma_1 - \sigma_2)^2 + (\sigma_2 - \sigma_3)^2 + (\sigma_3 - \sigma_1)^2]}$$

Where  $\sigma_1$ ,  $\sigma_2$ , and  $\sigma_3$  are the principle stresses in each grain. Examples of histograms showing the distribution of equivalent stress in the compression and transverse direction populations for an EPSC simulation that combines  $\{011\}[100]$  and  $\{110\}[001]$  slip are plotted in Figure 11. Several things are apparent from examining the simulation in this way. First as expected, stress states for grains contributing to reflections measured in the compression direction are much more strongly peaked than that of grains contributing to the transverse reflection. Second, the relationship between the stress levels measured in the compression direction and the stresses experienced by the population of grains producing the transverse reflections varies from reflection to reflection. For some reflections [e.g., (131) in this simulation] the equivalent stress in the compression direction population is significantly lower than the average stress state found in the transverse direction population. For other reflections [e.g., (002)], stress in the population reflecting in the compression direction is higher than the average of stress states in the transverse population. From these observations it should be clear, that the current

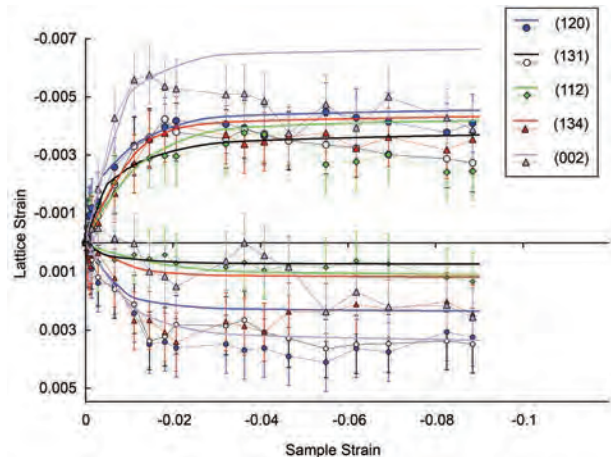


**FIGURE 9.** EPSC simulation Fay33-11 compared to lattice strains from experiment Fay\_33 (682 °C). The simulated lattice strains match the measured lattice strains to within measurement error for the all reflections in the compression direction during some point in the experiment. Lattice strains for the (002) and (131) reflections drop after the first 2% strain, a behavior that the simulation is not capable of matching. The match of the simulation to the lattice strains in the transverse direction is not as good, as discussed in the text.



**TABLE 3.** Comparison of macroscopic stress estimates

<i>hkl</i>	Fay_37 differential stress (GPa)	Fay_33 differential stress (GPa)
(021)	-2.87	
(131)	-3.17	-0.6583
(112)	-2.51	-0.4116
(101)	-2.93	
(120)	-2.40	-0.8867
(002)	-1.15	-0.6487
(134)		-0.6449
Average	-2.50	-0.6504
EPSC	-2.77/-2.70	-0.71

Notes: Stress estimates calculated for each measured reflection using the method of Singh et al. (1998) compared with macroscopic load calculated from EPSC simulations given in Table 2.

practice of taking *d*-spacings measured from the transverse and compression direction populations and using their differential along with a diffraction elastic constant to obtain stress is problematic because the differential is being calculated between the maximum and minimum components of two different stress states. In addition, because there can be a wide variation of stress states among grains that contribute to the transverse reflections, if any individual grain dominates diffraction, these reflections may well yield highly variable results. For all these reasons, it is therefore not advisable to calculate differential lattice strains but to consider each data set separately.

The author has recently put forth the hypothesis that the distribution of stress in polycrystals is best described as a percolation problem (Burnley 2013). The EPSC model and percolation models focus on two different aspects of the stress state inside of polycrystalline materials, but are not necessarily incompatible. By its nature the EPSC focuses on the average behavior of grain populations as defined by their orientation. The X-ray diffraction peak position is also a measure of average behavior. The percolation model, which includes short- and long-range grain-grain interactions, highlights spatial patterns in stress and strain and the degree of variation away from average. Variations in the stress state within a group of diffracting grains will produce peak broadening, which was not examined in this study.

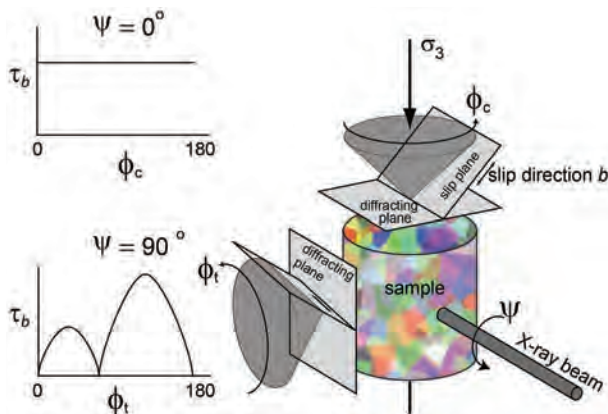


**FIGURE 10.** Diagram illustrating the relationship between the diffraction geometry for grains contributing to a given reflection and the orientation of a slip system within those grains. All grains contributing to the reflection in the vertical detector will experience the same resolved shear stress, where grains reflecting into the horizontal detector will experience various resolved shear stresses depending on their grain orientation.

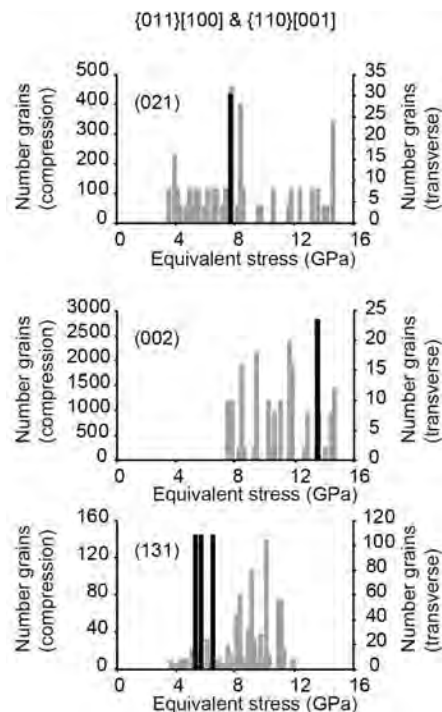


**FIGURE 11.** Histograms of equivalent stress in grains contributing to the (021), (002), and (131) reflections for an EPSC simulation of {011} [100] and {110}[001] slip.

## IMPLICATIONS

This study demonstrates that EPSC models can be used to successfully model in situ diffraction from deforming olivine if all the active deformation mechanisms are included in the model. The value in using an EPSC model to interpret diffraction from in situ deformation experiments is that the model allows plastic deformation mechanisms to be identified and produces a single macroscopic stress that is consistent with all of the diffraction data. The study also demonstrates the importance of kink band formation in olivine as an accommodation mechanism, as suggested by earlier work (Burnley et al. 2013). Including kink band formation to close the yield surface in VPSC models, which are used to model mantle rheology and interpret the development of lattice preferred orientation in the mantle (Castelnau et al. 2008), may improve their performance as well.

## ACKNOWLEDGMENTS

This work was supported by National Science Foundation grant EAR-0652894 and by the National Nuclear Security Administration under the Stewardship Science Academic Alliances program through DOE Cooperative Agreement no. DE-NA0001982. Use of the National Synchrotron Light Source, Brookhaven National Laboratory, was supported by the U.S. Department of Energy, Office of Science, Office of Basic Energy Sciences, under Contract No. DE-AC02-98CH10886 and use of the X17B2 beamline was partially supported by the Consortium for Materials Properties Research in Earth Sciences under NSF Cooperative Agreement EAR 06-49658. The author thanks Mike Brawner, Greg Hoth, and Chris Cline for assistance with data collection and analysis as well as Liping Wang for assistance on the beamline. The author also acknowledges Carlos Tome and Don Weidner for useful discussions as well as David Kohlstedt and an anonymous reviewer for their thoughtful and helpful reviews of the manuscript

## REFERENCES CITED

- Ave Lallemand, H.G. (1985) Subgrain rotation and dynamic recrystallization of olivine, upper mantle diapirism, and extension of the basin-and-range province. *Tectonophysics*, 119, 89–117.
- Budynas, R.G. (1999) *Advanced Strength and Applied Stress Analysis*, 2nd ed., 935 p. McGraw Hill, New York.
- Burnley, P.C. (2013) The importance of stress percolation patterns in rocks and other polycrystalline materials. *Nature Communications*, 4, 2117.
- Burnley, P.C., and Zhang, D. (2008) Interpreting in situ X-ray diffraction data from high pressure deformation experiments using elastic-plastic self-consistent models: An example using quartz. *Journal of Physics-Condensed Matter*, 20, 285201.
- Burnley, P.C., Cline, C.J., and Drue, A. (2013) Kinking in Mg<sub>2</sub>GeO<sub>4</sub> olivine: An EBSD study. *American Mineralogist*, 98, 927–931.
- Carter, N.L., Raleigh, C.B., and DeCarli, P. (1968) Deformation of olivine in stony meteorites. *Journal of Geophysical Research*, 73, 5439–5461.
- Castelnaud, O., Blackman, D.K., Lebensohn, R.A., and Castaneda, P.P. (2008) Micromechanical modeling of the viscoplastic behavior of olivine. *Journal of Geophysical Research-Solid Earth*, 113, B09202.
- Chen, J.H., Li, L., Yu, T., Long, H.B., Weidner, D., Wang, L.P., and Vaughan, M. (2006) Do Reuss and Voigt bounds really bound in high-pressure rheology experiments? *Journal of Physics-Condensed Matter*, 18, S1049–S1059.
- Daymond, M.R. (2006) Internal stresses in deformed crystalline aggregates. *Neutron Scattering in Earth Sciences*, 63, 427–458.
- Durham, W.B., Weidner, D.J., Karato, S.I., and Wang, Y.B. (2002) New developments in deformation experiments at high pressure. In S. Karato and H.R. Wenk, Eds., *Plastic Deformation of Minerals and Rocks*, 51, p. 21–49. Reviews in Mineralogy and Geochemistry, Mineralogical Society of America, Chantilly, Virginia.
- Durham, W.B., Mei, S., Kohlstedt, D.L., Wang, L., and Dixon, N.A. (2009) New measurements of activation volume in olivine under anhydrous conditions. *Physics of the Earth and Planetary Interiors*, 172, 67–73.
- Eshelby, J.D. (1957) The determination of the elastic field of an ellipsoidal inclusion, and related problems. *Proceedings of the Royal Society of London Series a—Mathematical and Physical Sciences*, 241, 376–396.
- Girard, J., Chen, J.H., Raterron, P., and Holyoke, C. (2010) Deformation of single crystal sample using D-DIA apparatus coupled with synchrotron X-rays: In situ stress and strain measurements at high pressure and temperature. *Journal of Physics and Chemistry of Solids*, 71, 1053–1058.
- Girard, J., Chen, J.H., Raterron, P., and Holyoke, C.W. (2013) Hydrolytic weakening of olivine at mantle pressure: Evidence of 100 (010) slip system softening from single-crystal deformation experiments. *Physics of the Earth and Planetary Interiors*, 216, 12–20.
- Hilairt, N., Wang, Y.B., Sanehira, T., Merkel, S., and Mei, S.M. (2012) Deformation of olivine under mantle conditions: An in situ high-pressure, high-temperature study using monochromatic synchrotron radiation. *Journal of Geophysical Research-Solid Earth*, 117, B01203.
- Hustoft, J., Amulele, G., Ando, J.-i., Otsuka, K., Du, Z., Jing, Z., and Karato, S.-i. (2013) Plastic deformation experiments to high strain on mantle transition zone minerals wadsleyite and ringwoodite in the rotational Drickamer apparatus. *Earth and Planetary Science Letters*, 361, 7–15.
- Isaak, D.G., Graham, E.K., Bass, J.D., and Wang, H. (1993) The elastic properties of single-crystal fayalite as determined by dynamical measurement techniques. *Pure and Applied Geophysics*, 141, 393–414.
- Karato, S.I. (2009) Theory of lattice strain in a material undergoing plastic deformation: Basic formulation and applications to a cubic crystal. *Physical Review B*, 79, 214106.
- Karato, S., and Weidner, D.J. (2008) Laboratory studies of the rheological properties of minerals under deep-mantle conditions. *Elements*, 4, 191–196.
- Kawazoe, T., Karato, S., Otsuka, K., Jing, Z.C., and Mookherjee, M. (2009) Shear deformation of dry polycrystalline olivine under deep upper mantle conditions using a rotational Drickamer apparatus (RDA). *Physics of the Earth and Planetary Interiors*, 174, 128–137.
- Kawazoe, T., Karato, S., Ando, J., Jing, Z.C., Otsuka, K., and Hustoft, J.W. (2010) Shear deformation of polycrystalline wadsleyite up to 2100 K at 14–17 GPa using a rotational Drickamer apparatus (RDA). *Journal of Geophysical Research-Solid Earth*, 115, B08208.
- Li, L., Weidner, D.J., Chen, J.H., Vaughan, M.T., Davis, M., and Durham, W.B. (2004) X-ray strain analysis at high pressure: Effect of plastic deformation in MgO. *Journal of Applied Physics*, 95, 8357–8365.
- Long, H., Weidner, D.J., Li, L., Chen, J., and Wang, L. (2011) Deformation of olivine at subduction zone conditions determined from in situ measurements with synchrotron radiation. *Physics of the Earth and Planetary Interiors*, 186, 23–35.
- Mei, S., Suzuki, A.M., Kohlstedt, D.L., Dixon, N.A., and Durham, W.B. (2010) Experimental constraints on the strength of the lithospheric mantle. *Journal of Geophysical Research-Solid Earth*, 115, B08204.
- Merkel, S., Tome, C., and Wenk, H.-R. (2009) Modeling analysis of the influence of plasticity on high pressure deformation of hcp-Co. *Physical Review B*, 79, 064110.
- Nishihara, Y., Tinker, D., Kawazoe, T., Xu, Y.S., Jing, Z.C., Matsukage, K.N., and Karato, S.I. (2008) Plastic deformation of wadsleyite and olivine at high-pressure and high-temperature using a rotational Drickamer apparatus (RDA). *Physics of the Earth and Planetary Interiors*, 170, 156–169.
- Oliver, E.C., Daymond, M.R., and Withers, P.J. (2004) Interphase and intergranular stress generation in carbon steels. *Acta Materialia*, 52, 1937–1951.
- Raleigh, C.B. (1968) Mechanisms of plastic deformation of olivine. *Journal of Geophysical Research*, 73, 5391–5406.
- Raterron, P., Amiguet, E., Chen, J., Li, L., and Cordier, P. (2009) Experimental deformation of olivine single crystals at mantle pressures and temperatures. *Physics of the Earth and Planetary Interiors*, 172, 74–83.
- Raterron, P., Chen, J., Li, L., Weidner, D., and Cordier, P. (2007) Pressure-induced slip-system transition in forsterite: Single-crystal rheological properties at mantle pressure and temperature. *American Mineralogist*, 92, 1436–1445.
- Raterron, P., Chen, J., Geenen, T., and Girard, J. (2011) Pressure effect on forsterite dislocation slip systems: Implications for upper-mantle LPO and low viscosity zone. *Physics of the Earth and Planetary Interiors*, 188, 26–36.
- Raterron, P., Girard, J., and Chen, J. (2012) Activities of olivine slip systems in the upper mantle. *Physics of the Earth and Planetary Interiors*, 200, 105–112.
- Raterron, P., Merkel, S., and Holyoke, C.W. III (2013) Axial temperature gradient and stress measurements in the deformation-DIA cell using alumina pistons. *Review of Scientific Instruments*, 84, 043906.
- Singh, A.K., Balasingh, C., Mao, H.K., Hemley, R.J., and Shu, J.F. (1998) Analysis of lattice strains measured under nonhydrostatic pressure. *Journal of Applied Physics*, 83, 7567–7575.
- Smyth, J.R., and Hazen, R.M. (1973) The crystal structures of forsterite and hortonolite at several temperatures up to 900 °C. *American Mineralogist*, 58, 588–593.
- Speziale, S., Duffy, T.S., and Angel, R.J. (2004) Single-crystal elasticity of fayalite to 12 GPa. *Journal of Geophysical Research-Solid Earth*, 109, B12202.
- Tome, C.N., and Oliver, E.C. (2002) Code elastio-plastic self-consistent (EPSC). Los Alamos National Laboratory, New Mexico.
- Turner, P.A., and Tome, C.N. (1994) A study of residual-stresses in ZIRCALOY-2 with rod texture. *Acta Metallurgica et Materialia*, 42, 4143–4153.
- Turner, P.A., Schristodoulou, N., and Tome, C.N. (1995) Modeling the mechanical response of rolled zircaloy-2. *International Journal of Plasticity*, 11, 251–265.
- Vaughan, M., Chen, J., Li, L., Weidner, D.J., and Li, B. (2000) Use of X-ray imaging techniques at high pressure and high temperature for strain measurements. In M.H. Manghnani, W.J. Nellis, and M.F. Nicol, Eds., *Science and Technology of High Pressure Proceedings of AIRAPT-17*, p. 1097–1098. Universities Press, Hyderabad, India.
- Wang, Y.B., Durham, W.B., Getting, I.C., and Weidner, D.J. (2003) The deformation-DIA: A new apparatus for high temperature triaxial deformation to pressures up to 15 GPa. *Review of Scientific Instruments*, 74, 3002–3011.
- Weidner, D.J., and Li, L. (2006) Measurement of stress using synchrotron X-rays. *Journal of Physics-Condensed Matter*, 18, S1061–S1067.
- Weidner, D.J., Vaughan, M.T., Wang, L.P., Long, H.B., Li, L., Dixon, N.A., and Durham, W.B. (2010) Precise stress measurements with white synchrotron X-rays. *Review of Scientific Instruments*, 81, 013903.

MANUSCRIPT RECEIVED OCTOBER 29, 2014

MANUSCRIPT ACCEPTED MARCH 18, 2015

MANUSCRIPT HANDLED BY MICHAEL GARCIA